RSC Advances

RSC Advances

www.rsc.org/advances

ROYAL SOCIETY OF CHEMISTRY

www.rsc.org/advances

Textual abstract

A yellow-orange emitting garnet phosphor $Mg_2Y_2Al_2Si_2O_{12}:Ce^{3+}$ was prepared through combination substitution and high colour rendering index white LED lamp was achieved.

Graphic abstract

RSC Advances
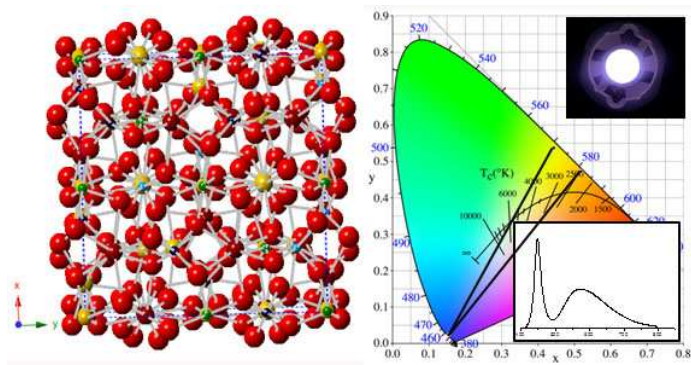
Combination cation substitution tuning of yellow-orange emitting phosphor $Mg_2Y_2Al_2Si_2O_{12}$:Ce^{3+}

Zaifa Pan,[*a] Yu Xu,[a] Qingsong Hu,[a] Weiqiang Li,[a] Huan Zhou[b] and Yifan Zheng[*a]

Cation substitution is a valuable approach to tune the crystal field splitting of garnet phosphor and hence enhance the red shift of the Ce^{3+} emission. A novel aluminate silicate garnet phosphor $Mg_2Y_2Al_2Si_2O_{12}$:Ce^{3+} is designed for the aim of a large distortion of the dodecahedron and an external pressure from the large octahedron through combination substitution of both dodecahedral Y^{3+} and octahedral Al^{3+} sites with Mg^{2+}. The garnet structure and elemental composition of this phosphor were confirmed by XRD, SEM and TEM. The particular coordination environment of each element of the phosphor was illustrated by XPS and Rietveld refinement. $Mg_2Y_{1.94}Al_2Si_2O_{12}$:$0.06Ce^{3+}$ exhibits a strong and broad yellow-orange emission band with CIE coordinate of (x = 0.519, y = 0.472) and shifts to red side of 57 nm, comparing with the commercial phosphor YAG:Ce^{3+}. This red-shift could be mainly ascribed to the distortion and shrinking of dodecahedron and subsequently the larger crystal field splitting of the Ce^{3+} 5d levels. White LED was fabricated and shows high colour rending index up to 84. These results reveal that Ce^{3+}-doped $Mg_2Y_2Al_2Si_2O_{12}$ phosphor is a promising blue light converted yellow-orange light emitting phosphor for white LED.

1 Introduction

White LED possesses the advantages of long working lifetime, high luminous efficiency, energy saving and environmental friendly, which make it become a potential candidate to replace the traditional incandescent and fluorescent lamp.[1-3] Since $Y_3Al_5O_{12}$:Ce^{3+} (YAG:Ce^{3+}) can absorb blue light and emit yellow light with high quantum efficiency (> 85%), Ce^{3+}-activated YAG has become the most important commercial yellow phosphor for blue LED chip.[4,5] However, the relative weak red component of the YAG:Ce^{3+} emission spectrum results in low colour rending index (Ra < 80) and high correlate colour temperature (CCT > 5000 K), which seriously limit its indoor lighting application.[6] Therefore, more and more attentions have been paid on the developing of new phosphors which emit longer wavelength light versus YAG:Ce^{3+} .

Besides the co-doping of other activator ions, including the Pr^{3+},[7] Sm^{3+},[8] Cr^{3+},[9] and Mn^{2+}–Si^{4+} pairs,[10] cation substitution is a useful approach to tune the crystal field splitting of the 5d orbit of Ce^{3+} and hence makes the emission shift to red side considerably. These modifications contain the direct substitution of dodecahedral activator ion sites with lager ion substituted $Tb_3Al_5O_{12}$:Ce^{3+},[11] and $Gd_3Al_5O_{12}$:Ce^{3+}.[12] The octahedral sites could also be substituted by the wide accepted strategy of replacing Al^{3+} (0.51 Å) by Mg^{2+} (0.66 Å)-Si^{4+} (0.42 Å) pair, which results in stronger crystal field splitting and a further shift of the Ce^{3+} emission to red side.[13,14] Quite recently, a double substitution of Mg^{2+}−Si^{4+}/Ge^{4+} replacing $Al(1)^{3+}$−$Al(2)^{3+}$ on octahedral and tetrahedral sites is reported and the red shift of the

emission is interpreted via the bond distance increasing in octahedron.[15] However, the correlationship between the luminescence shifts with the crystallography of these substitutions is still unclear, except for the phenomenological design rules of cation size effects.[14] On the other hand, besides this cation size effects on the redshift, Cheetham et al. preferred to the distortion factor of the dodecahedral doping site.[16,17] Furthermore, Seshadri group revealed that the compression of the Ce^{3+} local environments is ascribing to the unusually large crystal-field splitting of garnet, through insight view of local environment of activator ions.[18]

Considering the factors mentioned above, one could be inspired that partly substitution of dodecahedral site with small ion radii directly may result in a compression environment for the activator ion Ce^{3+} and large distortion of the dodecahedron, hence strong crystal field splitting. Meantime, the large octahedron may provide an external pressure on the activator centre dodecahedron and could further enhance the crystal fields splitting. Based on the above design rule, the combination cation substitution tuning garnet phosphor $Mg_2Y_2Al_2Si_2O_{12}$:Ce^{3+} is proposed. Herein, Mg^{2+} is predicted to incorporate both in dodecahedral Y^{3+} and octahedral Al^{3+} sites. Subsequently large distortion dodecahedron and big octahedron could be built up and longer wavelength emission is expected.

In this article, a novel Ce^{3+}-doped garnet phosphor $Mg_2Y_2Al_2Si_2O_{12}$ was synthesized by traditional solid state reaction with relative low temperature. The crystal structure and the particular coordination environment of each element were illustrated

by XRD, TEM and XPS. Intense yellow-orange emission was observed for the synthesized phosphor and the effect of crystal structure parameters of $Mg_2Y_2Al_2Si_2O_{12}$ on such red shift was discussed. White LED (WLED) was fabricated and the colorimetric properties were evaluated.

2 Experiment

A series of samples $Mg_2Y_{2-x}Al_2Si_2O_{12}:xCe^{3+}$ with different Ce^{3+} concentrations (x = 0, 0.01, 0.03, 0.06, 0.09 and 0.12) were synthesized by traditional solid state reaction method. Y_2O_3 (99.99%), MgO (99.5%), SiO_2 (99.99%), Al_2O_3 (99%) and CeO_2 (99.9%) were used as raw materials, and mixed uniformly in an agate mortar. Then, the precursor mixture was fired at 900 °C for 8 h in air in an alumina crucible. After the samples cooled down to room temperature and ground again into powder, the as-obtain precursor was sintered under a reducing atmosphere of 5% H_2: 95% N_2 at 1350 °C for 10 h. The products $Mg_2Y_{2-x}Al_2Si_2O_{12}:xCe^{3+}$ were allowed to cool down to room temperature in the furnace in reducing atmosphere, then ground and pulverized for further measurements.

The phase composition of the obtained powder samples were characterized by X-ray diffraction (XRD) analysis on PNAlytical X'Pert Pro diffractometer with Cu Kα radiation at 40 mA and 40 kV in 2θ range from 5°to 125° with scanning step of 0.0167°. Rietveld structural refinement was done by General Structure Analysis System (GSAS) software package. The particle size, morphology and the content of each element were observed by scanning electron microscope (SEM, Hitachi S-4700Ⅱ) with accelerating voltage 15 kV which had an energy-dispersive x-ray spectrometer (EDX) attachment. High-resolution and elemental mapping analysis of sample were operated under a high-angle annular dark field mode by scanning transmission electron microscope (STEM, FEI Tecnai G2 F30 S-TWIN) with accelerating voltage 300 kV. X-ray photoelectron spectroscopy (XPS) measurement was performed using an Axis Ultra DLD spectrometer (Kratos Analytical). The instrument was equipped with a monochromatized aluminum X-ray source powered at 15 kV and 3 mA that delivered an X-ray beam of 300 μm × 700 μm. Charge compensation was obtained with the built in charge neutralization system. The pass energy was set to 160 eV for the survey spectra and for the high-resolution spectra, the pass energy of Al 2p, Si 2p and Y 3d are 40 eV, 40 eV and 20 eV, respectively. The binding energies were calculated with respect to the C component (BE = 284.8 eV) of the C1s peak, and a Shirley background subtraction was used. For the spectrum fitting, an XPS analysis program Xps peak 4.1 was used, and a Lorentz–Gauss algorithm was applied. The fitted peak positions were compared with those reported in the literatures and full width half maximum (FWHM) of all the peaks was also used to evaluate the reasonableness of the fitting results. The photoluminescence (PL) and photoluminescence excitation (PLE) spectra were recorded on Fluoromax-4 (JOBIN YVON) equipped with a 150 W xenon lamp as the excitation light source. Cut-off filter was used in the measurements to eliminate the second-order bands of the source radiation. The temperature-dependent emission spectra were recorded using a Fluoromax-4 spectrophotometer equipped with a

heater (TAP-02, Orient Koji Scientific) in the sample compartment. PL spectra of all the samples were recorded three times and averaged to reduce the error. The quantum efficiency was measured using the same fluorescent spectrometer (Fluoromax-4) with an integrating sphere (F3018) accessory. The electroluminescence spectra of phosphor-converted WLED were measured by using a UV-VIS-near IR Spectrophoto Colormeter (PMS-80, EVERFINE PHOTO). All measurements were performed at room temperature. The commercial phosphor YAG:Ce^{3+} was provided by HangZhou Ying-he Optoelectronic Technology Co.,LTD (YH-Y552M). And the Blue LED chip (455nm) was purchased from JiangXi Yuan-en Optoelectronic Technology Co.,LTD. The chip size is 45*45 mil and the nominal voltage range is 3.4 ~ 3.6V.

3 Rustles and discussion

3.1 Crystal structure of the host $Mg_2Y_2Al_2Si_2O_{12}$.

The X-ray diffraction pattern of the host $Mg_2Y_2Al_2Si_2O_{12}$ is shown in Figure 1. The main diffraction peaks of the sample are in accordance with the standard diffraction peaks of $Y_3Al_5O_{12}$ (No. 088-2048), demonstrating that $Mg_2Y_2Al_2Si_2O_{12}$ is cubic with the space group Ia-3d. And the strong diffraction peaks at 2θ = 33.4° and 18.2° are attributed to (420) and (210) crystal planes, respectively. The peak marked with asterisk is belong to the competition second phase of $Y_{4.67}(SiO_4)_3O$ (No. 30-1457), which is also observed as second phase for the phosphor $Lu_2CaMg_2(Si,Ge)_3O_{12}:Ce^{3+}$.[14] Similar to the conclusion of Setlur,[14] the phase of $Y_{4.67}(SiO_4)_3O$ with apatite structure will not influence the photoluminescence properties of phosphor $Mg_2Y_2Al_2Si_2O_{12}:Ce^{3+}$. In addition, the diffraction peaks of the host $Mg_2Y_2Al_2Si_2O_{12}$ are very sharp and strong, suggesting that a good crystallinity of phosphor can be obtained through this method. And it is very important for phosphor, because better crystallinity means less traps and stronger luminescence.
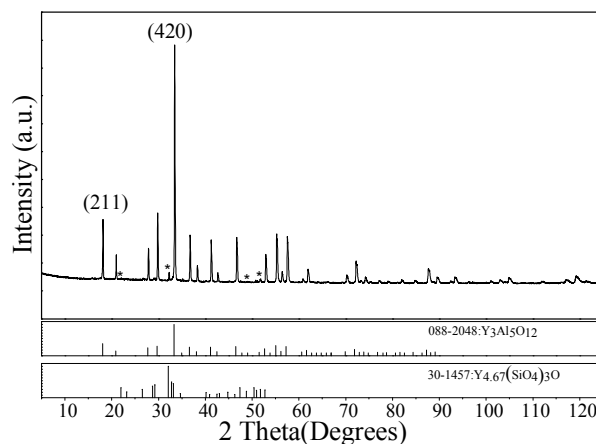

Fig. 1 XRD patterns of the host $Mg_2Y_2Al_2Si_2O_{12}$, standard card No. 088-2048 ($Y_3Al_5O_{12}$) and No. 30-1457($Y_{4.67}(SiO_4)_3O$).

The morphology is characterized by SEM and the phosphors consist of many irregular granular microcrystals with particle size of 10-20 μm, which is shown in figure S1. EDX is used to determine the stoichiometric ratio of each element of the synthesized samples.

And the measurement results are shown in Table 1. The sample is mainly composed of Mg, Y, Al, Si and O and the atomic ratio is in accordance with the theoretical composition 1:1:1:1:6 of the sample. Similar composition is detected for the different surface sites of the powder, indicating that each element distributes uniformly in the sample. From the picture of high resolution transmission electron microscopy (HRTEM), the interplanar distance between adjacent lattice fringes are determined to be 0.27 nm and 0.5 nm (Figure 2a). The corresponding 2θ value could be calculate by the Bragg's equation $n\lambda=2d\sin\theta$, where λ is the X-ray wavelength, d is the distance between two crystal planes, and θ is the diffraction angle of an observed peak. According to the equation, the calculated 2θ results were 33.2° and 17.7°, respectively, which are close to the 2θ value of (420) and (210) crystal planes (2θ = 33.4° and 18.2°) obtained by XRD. These indicate that the lattice fringes shown in Figure 2a are belong to (420) and (210) crystal planes. The energy dispersive X-ray mapping performed by scanning transmission
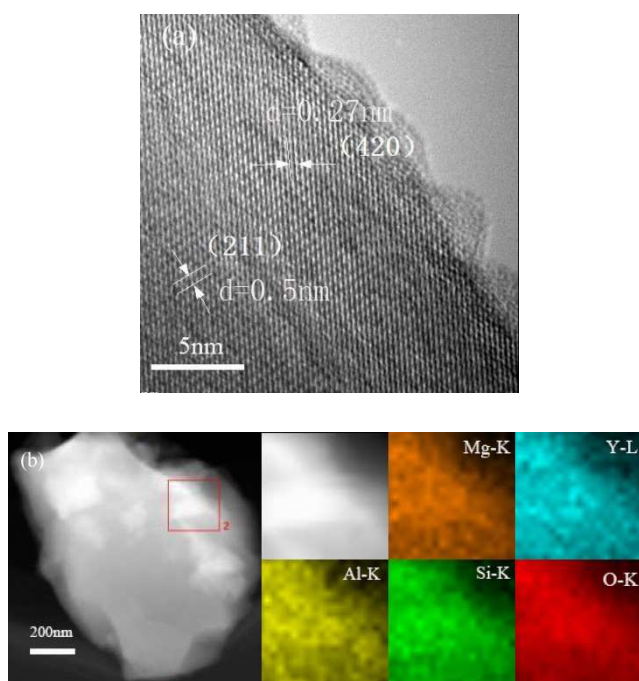

Fig. 2 HRTEM image (a) and element distribution mapping (b) of the host $Mg_2Y_2Al_2Si_2O_{12}$.

Table 1 EDX results of the element contents inthe host $Mg_2Y_2Al_2Si_2O_{12}$

Element	Wt%	At%
Mg(K)	6.75	7.56
Al(K)	10.03	10.13
Si(K)	11.06	10.73
Y (L)	34.32	10.51
O (K)	35.61	61.63

electron microscope has been carried out to further confirm the element composition and the uniform distribution of elements. As shown in Figure 2b, the phosphor is composed of Mg, Y, Al, Si and

O and the distribution of Mg, Y, Al, Si and O elements is homogeneous in the phosphor, which agree well with the results measured by EDX.

To illustrate the particular coordination sites of each element occupied in garnet structure for the present novel host, XPS is used to confirm the chemical states of each element. The XPS survey scan is exhibited in Figure 3a, suggesting that the host contains Mg, Y, Al, Si and O elements. Figure 3b shows the high resolution XPS analysis of variation in Al 2p peak. The Al 2p peak is broad and can be roughly de-convoluted into two peaks, one at lower binding energy 73.7 eV and the other at slightly higher binding energy 75.3 eV, which belong to $[AlO_4]$ tetrahedral and $[AlO_6]$ octahedral coordination, respectively.[19-21] The Si 2p XPS peak is displayed in Figure 3c with two peaks which could be assigned to the Si $2p_{1/2}$ and Si $2p_{3/2}$ of $[SiO_4]$, proving that Si is in the form of $[SiO_4]$ existing in the structure of $Mg_2Y_2Al_2Si_2O_{12}$.[22,23] In addition, the two peaks of Y 3d can be well fitted to the 3d orbit of Y splitting of $3d_{3/2}$ and $3d_{5/2}$, indicating that the Y exists as one type of dodecahedral coordination in $Mg_2Y_2Al_2Si_2O_{12}$.[24] The XPS data of Mg^{2+} could be fitted into two peaks, i.e., two kinds of the chemical states and occupy the left dodecahedral and octahedral sites of garnet structure. From above-mentioned, Mg^{2+} is incorporated into both dodecahedral Y^{3+} and octahedral Al^{3+} sites successfully and the chemical formula of $Mg_2Y_2Al_2Si_2O_{12}$ could be represented as $\{Y_2Mg\}[MgAl](AlSi_2)O_{12}$, where the { }, [] and () donate dodecahedral, octahedral and tetrahedral coordination, respectively. In conclusion, the XPS results provide additional evidence for the formation of the garnet structure $Mg_2Y_2Al_2Si_2O_{12}$.
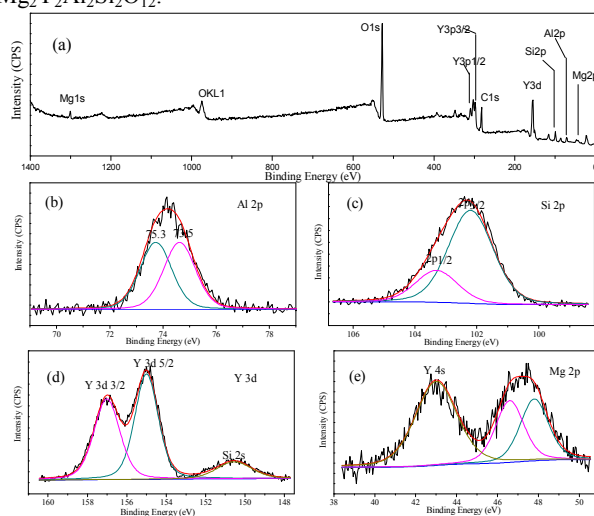

Fig. 3 XPS survey scan (a) and high-resolution Al 2p (b), Si 2p (c), Y 3d (d) and Mg 2p (e) XPS spectra of the host $Mg_2Y_2Al_2Si_2O_{12}$.

Crystal structure refinement is a powerful tool to get detail crystal structure information of $Mg_2Y_2Al_2Si_2O_{12}$ and ensure the phase purity of the sample. Based on the results of XPS, the atom positions are set as following: Y^{3+} and half of Mg^{2+} occupy the dodecahedral sites, and the octahedral sites are occupied by the rest of Mg^{2+} and half of

Al^{3+}, and the tetrahedral sites are occupied by Si^{4+} and the rest of Al^{3+}. Moreover, as no structure detail of $Y_{4.67}(SiO_4)_3O$ was reported, the crystallographic data of $Gd_{4.67}(SiO_4)_3O$, which has the same structure as the $Y_{4.67}(SiO_4)_3O$, was used as the starting model.[25]
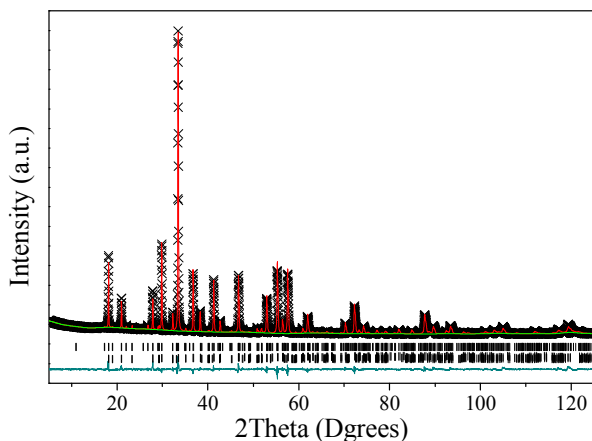
Fig. 4 XRD profiles for Rietveld refinement result of $Mg_2Y_2Al_2Si_2O_{12}$ and $Y_{4.67}(SiO_4)_3O$. Observed intensities (cross), calculated patterns (red line), Bragg positions (tick mark), and difference plot (blue line) are presented.

Table 2 Crystallographic data, atomic coordinates and isotropic parameters of $Mg_2Y_2Al_2Si_2O_{12}$ and $Y_{4.67}(SiO_4)O$ by Rietveld refinement

Atom	x/a	y/b	z/c	S.O.F.	U($Å^2$)
$Mg_2Y_2Al_2Si_2O_{12}$[a]					
Al	0	0	0	0.50	0.03418
Mg	0.25	0.125	0	0.33	0.01919
Y	0.25	0.125	0	0.67	0.01919
Si	0.25	0.375	0	0.67	0.03619
O	0.032	0.053	0.65	1.00	0.03563
Al	0.25	0.375	0	0.33	0.03619
Mg	0	0	0	0.5	0.03418
$Y_{4.67}(SiO_4)O$[b]					
Y	0.2270	0.2289	0.75	1	0.03233
Y	0.6667	0.3333	0	1	0.03458
Si	0.4714	0.3884	0.25	1	0.06273
O	0.3178	0.4872	0.25	1	0.06742
O	0.6002	0.4740	0.25	1	0.02195
O	0.3418	0.2497	0.0575	1	0.07056
O	0	0	0.25	1	0.04281

a Cubic; space group:Ia-3d;lattice parameters: a=11.972 Å V=1715.76 Å^3; α = β = γ = 90°; T = 298K; Z = 8.b Hexagonal; space group: P63/m; lattice parameters: a a=b=9.3294 Å, c = 6.661Å,V= 579.51Å3; α = β = 90°, γ = 120°; T = 298K; Z = 2.Cu Kα, λ = 1.5418; total reflections = 7171.

O Y Mg Al(6) Al(4) Si
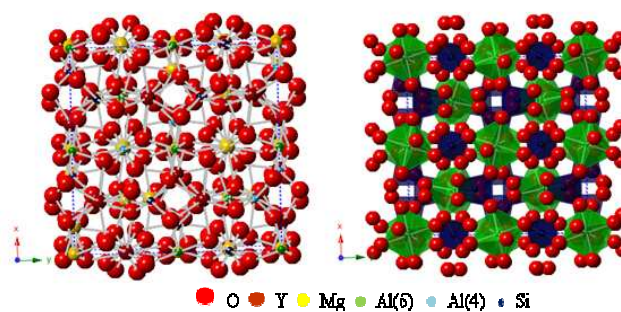
Fig. 5 Crystal structure of the host $Mg_2Y_2Al_2Si_2O_{12}$ along the z-axis direction.

Figure 4 shows the Rietveld refinement result of $Mg_2Y_2Al_2Si_2O_{12}$ with the final converged weighted-profile of Rwp = 4.00%, by indexing to two phases of YAG and $Gd_{4.67}(SiO_4)_3O$. The refine results show that the main phase of the prepared sample is garnet with the phase content of 95.6%. The crystallographic data, atomic coordinates and isotropic parameters of the final refinement of $Mg_2Y_2Al_2Si_2O_{12}$ and $Y_{4.67}(SiO_4)_3O$ are summarized in Table 2. The well converged Rietveld refinement is a further proof of the designed element occupancy and formation of the garnet structure $\{Y_2Mg\}[MgAl](AlSi_2)O_{12}$.

The garnet crystal structure of $Mg_2Y_2Al_2Si_2O_{12}$ is shown in the Figure 5, which can be depicted as a network of octahedral and tetrahedral connected by sharing oxygen ions at the corners of the polyhedral. These polyhedral are arranged in chains along the three crystallographic directions and form dodecahedral cavities which are occupied by the Y^{3+} and Mg^{2+} ions. On the basis of ionic radii in the $Mg_2Y_2Al_2Si_2O_{12}$ lattice, the Ce^{3+} ions are considered to mainly occupy the distorted dodecahedral sites by substituting the Y^{3+} ions and to be coordinated by eight O^{2-} ions. The interatomic distances in $Mg_2Y_2Al_2Si_2O_{12}$ are listed in Table 3 and the change versus that in YAG are in accordance with the ionic radii of the substitute element in each polyhedral. The decreasing of Y-O bond distance could be attributing to the substitution of the dodecahedral sites with the smaller Mg^{2+} ion, as well as the compression effect from the bigger neighbor octahedron. Furthermore, according to the interatomic distance, the difference of the bond length between the two kinds of Y-O in the host $Mg_2Y_2Al_2Si_2O_{12}$ is greater than that in YAG, suggesting that the dodecahedral become more distorted and red-shift of Ce^{3+} emission is expected.

Table 3 Selected interatomic bond distances of $Mg_2Y_2Al_2Si_2O_{12}$[a]

	$Mg_2Y_2Al_2Si_2O_{12}$	$Y_3Al_5O_{12}$
Y-O	2.294	2.317
Y-O	2.417	2.437
Al-O(6)	1.992	1.938
Al-O(4)	1.715	1.754
Mg-O(8)	2.294	
Mg-O(8)	2.417	
Mg-O(6)	1.992	
Si-O	1.715	

a Bond distances in Å
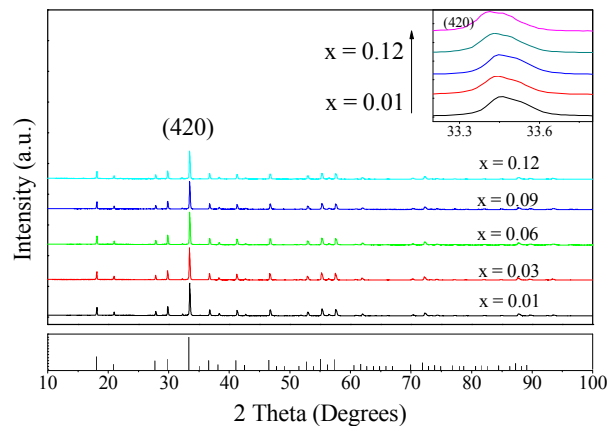
ig.6 XRD patterns of the phosphors $Mg_2Y_{2-x}Al_2Si_2O_{12}$:$xCe^{3+}$ (x = 0.01, 0.03, 0.06, 0.09 and 0.12). The inset displays an enlargement of the XRD patterns showing the shift of the XRD peak (420) on Ce^{3+} doping concentration.

Table 4 Calculated unit cell parameters of the phosphors $Mg_2Y_{2-x}Al_2Si_2O_{12}$:$xCe^{3+a}$

	Z=0.01	Z=0.03	Z=0.06	Z=0.09	Z=0.12
a=b=c(Å)	11.973	11.975	11.976	11.980	11.982
Cell volumn(Å^3)	1716.36	1717.22	1717.65	1719.37	1720.24
χ^2	6.23	6.45	4.69	6.58	6.76
Rwp(%)	5.19	5.33	4.75	5.53	5.68
Rp(%)	3.47	3.61	3.30	3.70	3.81

^{a}Crystal system: cubic, space group:Ia-3d (No. 088-2048).

Fig. 6 illustrates the XRD pattern of phosphors $Mg_2Y_2Al_2Si_2O_{12}$ with different doping concentration of Ce^{3+} ion. It is obvious that the diffraction peaks of the samples cohere with the peaks of $Y_3Al_5O_{12}$. However, all diffraction peaks slightly shift to low angle, manifesting that Ce^{3+} ion has been effectively doped into the matrix lattice of $Mg_2Y_2Al_2Si_2O_{12}$. Because the replacement of Y^{3+} by lager radius Ce^{3+} results in bigger d-spacing, and the diffraction peaks shift to the low angle according to the Bragg's equation. Meanwhile, with the doping concentration of Ce^{3+} ion increases, diffraction peaks consistently shift to the low angle (see the inset of Figure 6), demonstrating that the more the Ce^{3+} ion doped into the matrix lattice, the larger the cell parameters will become. Table 4 reveals such relationship that the lattice parameters and cell volumes increase gradually with Ce^{3+} ions increasing for all the samples, which is calculated by cell refinement fitting with GSAS on the base of XRD data.[26]

3.2 Photoluminescence properties of phosphor $Mg_2Y_2Al_2Si_2O_{12}$:Ce^{3+}.

Figure 7 displays the PLE (λ_{em} = 599 nm) and PL spectra (λ_{ex} = 460 nm) of phosphor $Mg_2Y_{1.94}Al_2Si_2O_{12}$:$0.06Ce^{3+}$. The emission spectrum of this phosphor has a broad emission peaking at 599 nm and shifts to red side for 57 nm, in comparison with 542 nm of YAG:Ce^{3+}. The position of the Ce^{3+} emission band depends on covalency (nephelauxetic effect), crystal field strength and Stokes Shift.[27] This red-shift could be mainly ascribed to the larger crystal field splitting of the Ce^{3+} 5d levels in the silicate garnet. In the as-synthesized phosphor, [Mg]-[Si] doping leads to the shrinking of tetrahedral and dodecahedral volumes, and the increasing of the octahedral volume. As shown in Table 3, in comparison with the cell volume and bond distance of YAG (V = 1731.85 Å^3, Y-O bond length: 2.317 Å, 2.437 Å), $Mg_2Y_2Al_2Si_2O_{12}$ possess relatively smaller volume of the unit cell (V = 1715.76 Å^3) and the smaller dodecahedral of [YO8] (Y-O bond length: 2.294 Å, 2.417Å). Thus, the shrinking of dodecahedral volumes will result in a stronger crystal field splitting and redder emission, when Ce^{3+} doped into the Y^{3+} site of phosphor $Mg_2Y_2Al_2Si_2O_{12}$. Meantime, because of the energy transfer between high energy and low energy part of Ce^{3+} ions emission, the Stokes shift of the Ce^{3+} emission in the garnet host may increase. The Stokes shift of phosphor $Mg_2Y_{1.94}Al_2Si_2O_{12}$:$0.06Ce^{3+}$ is 5100 cm^{-1}, which is larger than that of YAG:Ce^{3+} (3220 cm^{-1}). The large Stokes shift of phosphor $Mg_2Y_{1.94}Al_2Si_2O_{12}$:$0.06Ce^{3+}$ is another factor accounting for the red shift of the yellow-orange light emission. Moreover, the emission bands in these samples are broader (FWHM = 159 nm) than that of YAG (FWHM = 116 nm), which is due to the inhomogeneous broadening. That is to say, different Ce^{3+} site environments occur in the garnet structure arising from the dodecahedral site disorder between Y^{3+} and Mg^{2+} in $Mg_2Y_{1.94}Al_2Si_2O_{12}$:$0.06Ce^{3+}$. The larger FWHM means larger spectral coverage, which leads to higher Ra. In addition, the emission spectrum can be decomposed into two overlapping Gaussian bands, indicating that the ground state energy level of 4f is split by the spin–orbit interaction into the $^2F_{5/2}$ and $^2F_{7/2}$ levels and the splitting value in host $Mg_2Y_2Al_2Si_2O_{12}$ is about 2300 cm^{-1}. This splitting value is larger than that of YAG, which is also due to the inhomogeneous broadening causing by the dodecahedral site disorder between Y^{3+} and Mg^{2+}. The excitation spectrum consists of two broad bands with the peaks at 360 nm and 460 nm, which are assigned to the 4f-5d electronic transitions of Ce^{3+} ion. From the excitation spectrum, the phosphor possesses a strong broad absorption band from 440 nm to 480 nm, indicating that the phosphor can be effectively excited by the blue light emitting diode chip.

The dependence of the emission intensities on Ce^{3+} doping concentration is shown in the Figure 8. The emission intensity increases with the increasing of Ce^{3+} content until reach a maximum at x = 0.06, and the emission intensity declines when the concentration of Ce^{3+} beyond 0.06 (also see the inset of Figure 8), because of the concentration quenching. Thus, the
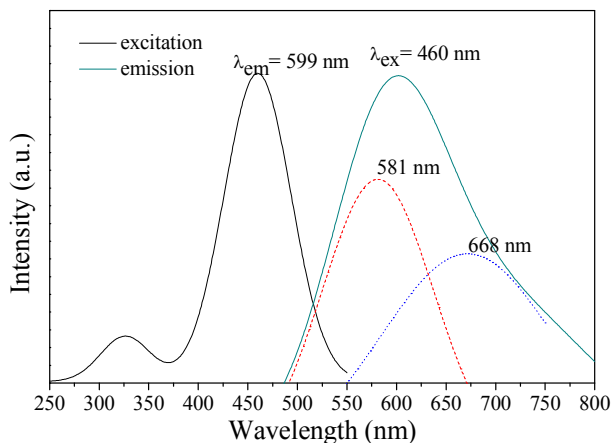
Fig. 7 PLE and PL spectra of phosphor $Mg_2Y_{1.94}Al_2Si_2O_{12}:0.06Ce^{3+}$.

optimal doping concentration of Ce^{3+} is 0.06. Furthermore, the inset of Figure 8 also shows the relationship of peak wavelength with Ce^{3+} doping concentration. With the increasing of doping concentration of Ce^{3+}, the emission spectra gradually shift to the red side with the wavelength from 584 nm for x = 0.01 to 617 nm for x = 0.12. This indicates that the crystal field splitting of the 5d energy level of Ce^{3+} ions increases with the increasing of Ce^{3+} concentration, which can be supported by the unit cell parameters in Table 4.

The concentration quenching could be ascribed to the energy transfer via one Ce^{3+} ion to another Ce^{3+} ion, which often occurs as a result of a radiation reabsorption, exchange interaction, or electric multipolar interaction. The mechanism of radiation reabsorption comes into effect only when there is a broad overlap of the spectra of the excitation and emission. As showed in the Figure 7, the overlap between the spectra of the excitation and emission is less than 2%, suggesting that the radiation reabsorption can be neglected. In this phosphor, when in low concentration, the average distance between the identical Ce^{3+} ions is so large that the energy migration is prohibited. The critical distance is of great importance which can be calculated with the following equation:

$$R_c \approx 2\left(\frac{3V}{4\pi x_c N}\right)^{\frac{1}{3}}$$

Where N is the number of cations in the unit cell, V is the volume of the unit cell and x_c is the critical concentration. Accoding to the formula of $Mg_2Y_{1.94}Al_2Si_2O_{12}:0.06Ce^{3+}$, the critical distance was determined to be 19.0 Å. The exchange interaction is generally responsible for the energy transfer of forbidden transitions and the typical critical distance is less than 5 Å. Therefore, the process of energy transfer between Ce^{3+} ions in phosphor $Mg_2Y_2Al_2Si_2O_{12}:Ce^{3+}$ should be controlled by the electric multipolar interaction according to Dexter's theory.[28,29]
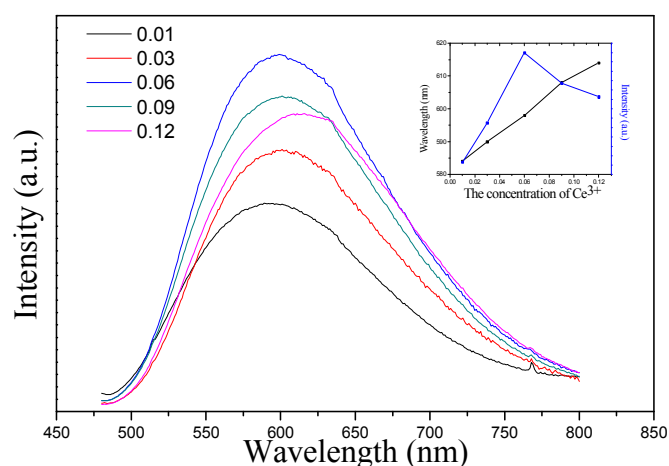

Fig. 8 Emission spectra of phosphors with different doping concentration. The inset displays the dependence of wavelength and the intensity of emission on the concentration of Ce^{3+}.

3.3 Temperature-dependent photoluminescence, CIE and quantum efficiency of phosphor $Mg_2Y_2Al_2Si_2O_{12}:Ce^{3+}$.

For the application in high power LEDs, thermal quenching property of phosphor is an important parameter to be considered. The thermal quenching of phosphor $Mg_2Y_{1.94}Al_2Si_2O_{12}:0.06Ce^{3+}$ is evaluated by measuring the temperature dependent emission from 25 °C up to 250 °C. Temperature dependent emission spectra for this phosphor under excitation at 460 nm are investigated and are shown in Figure 9. With the temperature increasing, the emission intensity remains in a relative stable value at first, and declined to 84.7% efficient at 160 °C comparing with T = 25 °C emission. The peak positions of the emission spectra slightly red shift and the peaks occur thermal broadening phenomenon.[30]
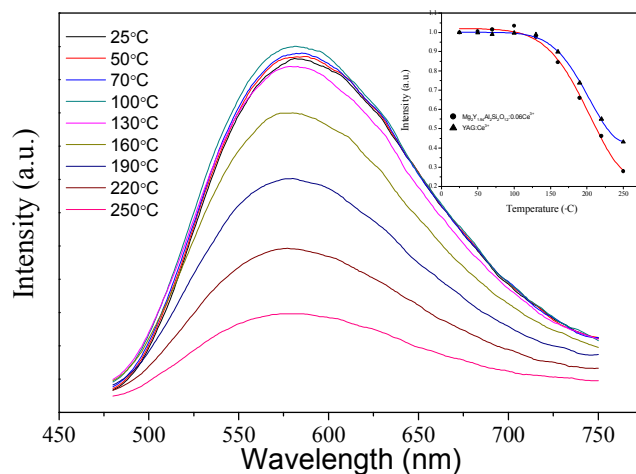

Fig. 9 Temperature-dependant photoluminescence of

$Mg_2Y_{1.94}Al_2Si_2O_{12}:0.06Ce^{3+}$ under excitation of 460nm.
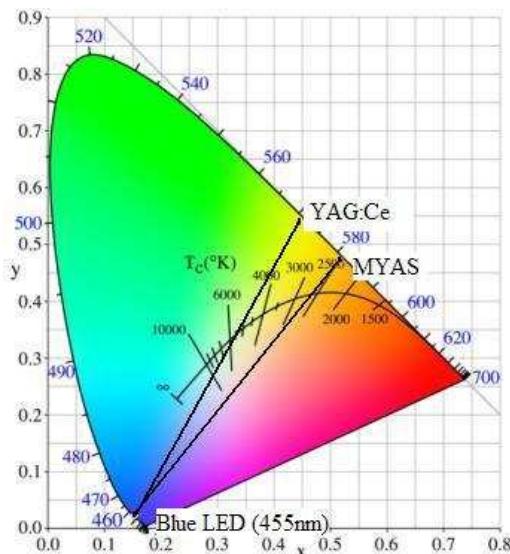
Fig. 10 CIE coordinates of the phosphor $Mg_2Y_{1.94}Al_2Si_2O_{12}:0.06Ce^{3+}$ and the commercial phosphor YAG:Ce^{3+}.

And the emission intensity of YAG:Ce^{3+} declines to 89% when the temperature increases to 160°C. The thermal stability of YAG:Ce^{3+} is better than that of $Mg_2Y_2Al_2Si_2O_{12}:Ce^{3+}$, The quenching activation energy (Ea, energy barrier for thermal quenching) will reduce, when the Stokes shift between 4f−5d absorption and 5d−4f emission gradually increases[15]. Because the Stokes shift of $Mg_2Y_2Al_2Si_2O_{12}:Ce^{3+}$ is larger than that of YAG:Ce^{3+}, the thermal quenching is more likely to occur.

The CIE chromaticity diagram for the sample $Mg_2Y_{1.94}Al_2Si_2O_{12}:0.06Ce^{3+}$ under excitation at 460 nm is shown in Figure 10. The colour coordinate of the present phosphor is (x = 0.519, y = 0.472) which is located at yellow-orange region, indicating that warm light with low CCT could be expected when coupling this yellow-orange light emitting phosphor with blue LED chip. The quantum efficiency (QE) of phosphor is considered as another important parameter for practical application and the main two factors for low quantum efficiency are concentration quenching and thermal quenching. The quantum efficiency data are measured for the phosphors with different Ce^{3+} doping concentration. And the quantum efficiency of phosphor $Mg_2Y_{1.94}Al_2Si_2O_{12}:0.06Ce^{3+}$ is measured to be 57% at room temperature. As a reference, the quantum efficiency value of the commercial yellow phosphor YAG:Ce^{3+} is measured with the same instruments, and the value is 73% under 460 nm excitation. Many factors will affect the QE, such as the excitation wavelength, the synthesis conditions and particle size, and further optimizing of the synthesis condition is necessary to improve the QE.

3.4 Electroluminescence properties of phosphor $Mg_2Y_2Al_2Si_2O_{12}:Ce^{3+}$.

.
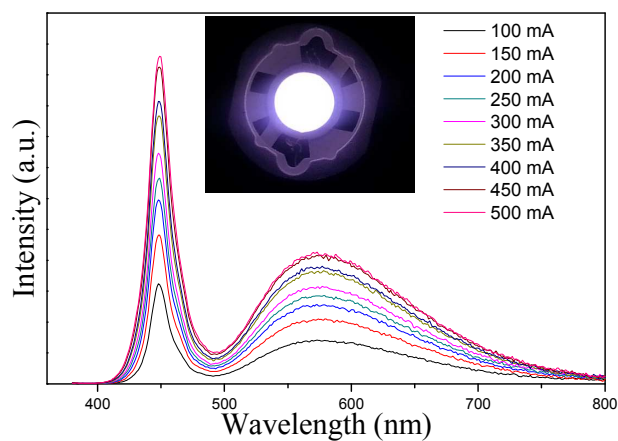
Fig. 11 Electroluminescent spectra of $Mg_2Y_{1.94}Al_2Si_2O_{12}:0.06Ce^{3+}$ phosphor-converted WLEDs under various drive currents from 100 mA to 500 mA.

Table 5 colour rendering index (Ra), colour coordinates and correlated colour temperature of the $Mg_2Y_{1.94}Al_2Si_2O_{12}:0.06Ce^{3+}$ phosphor-converted WLED under various currents

Current (mA)	Coordinate	CCT (K)	CRI(Ra)	Luminous efficacy (lm/W)
100	(0.3493, 0.3129)	4620	81.0	27.54
150	(0.3466, 0.3097)	4730	81.2	26.31
200	(0.3436, 0.3061)	4860	81.6	23.42
250	(0.3414, 0.3035)	4967	82.0	20.47
300	(0.3389, 0.3001)	5091	82.4	18.30
350	(0.3368, 0.2975)	5206	82.7	17.68
400	(0.3343, 0.2946)	5356	83.3	15.87
450	(0.3306, 0.2896)	5599	84.2	15.20
500	(0.3279, 0.2863)	5796	84.7	13.56

To study the practical application of $Mg_2Y_2Al_2Si_2O_{12}:Ce^{3+}$ for a phosphor–converted white LED, the LED lamps are fabricated by using phosphor $Mg_2Y_{1.94}Al_2Si_2O_{12}:0.06Ce^{3+}$ with blue InGaN chips (455 nm).The electroluminescence spectra of the obtained LED lamp are shown in the Figure 11. Bright white light is observed with naked eye and the inset of Figure 11 shows the photograph of the lamp with driven forward bias DC current of 300 mA. The colour rendering index, chromaticity coordinates, correlated colour temperature and luminous efficacy of $Mg_2Y_2Al_2Si_2O_{12}:Ce^{3+}$ are 82.4, (0.3389, 0.3001), 5091K and 18.30 lm/W, respectively, indicating that $Mg_2Y_2Al_2Si_2O_{12}:Ce^{3+}$ phosphor-converted white LED has high CRI and low CCT. However, the luminous efficacy is low, which is due to the relative low quantum efficiency and the irregular shape of the particles with large size distribution. Further improvement of conversion efficiency is possible by optimization of lamp fabrication and phosphor synthesis. For application in high power LEDs, the effect of current stability on the light output and CRI of the phosphor

should be considered. The current is tested from 100 mA to 500 mA to power the LED device. The electroluminescence properties, including the colour rendering index, chromaticity coordinates and correlated colour temperature are listed in Table 5. From Figure 11, it can be seen that the shift of emission peak is negligible and the intensity do not become saturated. Meanwhile, colour rendering index, chromaticity coordinates and correlated colour temperature change slightly as the current increasing. These results reveal that the phosphor-converted white LEDs are stable for application.

4 Conclusions

In conclusion, a novel Ce^{3+}-activated yellow-orange light emitting phosphor $Mg_2Y_2Al_2Si_2O_{12}$ is prepared by combination substitution of both dodecahedral Y^{3+} and octahedral Al^{3+} sites with Mg^{2+}. The crystal structure of the host $Mg_2Y_2Al_2Si_2O_{12}$ is illustrated to be $\{Y_2Mg\}[MgAl](AlSi_2)O_{12}$, where the { }, [] and () donate dodecahedral, octahedral and tetrahedral coordination, respectively. Moreover, the large distortion of the dodecahedron and an external pressure from the large octahedron lead to a large crystal field splitting and hence $Mg_2Y_{1.94}Al_2Si_2O_{12}:0.06Ce^{3+}$ shows a broad emission band with CIE chromaticity coordinates (x = 0.519, y = 0.472). Owing to the larger FWHM and redshift of emission band, high colour rendering index white LED lamp was achieved by combining the phosphor $Mg_2Y_2Al_2Si_2O_{12}:Ce^{3+}$ with a blue LED chip. Our results demonstrate that phosphor $Mg_2Y_2Al_2Si_2O_{12}:Ce^{3+}$ is a promising candidate for WLED.

Acknowledgements

Notes and references

[a] College of Chemical Engineering, Zhejiang University of Technology, Hangzhou 310014, P.R. China. E-mail: panzaifa@zjut.edu.cn

[b] Research Center of Analysis and Measurement, Zhejiang University of Technology, Hangzhou 310014, P.R. China.

1 J. Zhou, Z. G. Xia, M. X. Yang and K. J. Shen,*J. Mater. Chem.*, 2012, **22**, 21935-21941.

2 Z. J. Zhang, O. M. T. Kate, A. C. A. Delsing, M. J. H. Stevens, J.T. Zhao, P. H. L. Notten, P. Dorenbos and H. Hintzen,*J. Mater. Chem.*, 2012, **22**, 23871-23876.

3 Y. M. Ji, D. Y. Jiang, L. S. Qin, J. J. Chen, T. Feng, Y. K. Liao, Y. P. Xu and L. J. Shi, *J. Cryst. Growth*, 2005, **280**, 93-98.

4 C. M. Liu, H. B. Liang, X. J. Kuang, J. P. Zhong, S. S. Sun and Y. Tao, *Inorg. Chem.*, 2012, **51**, 8802-8809.

5 X. J. Wang, G. H. Zhou, H. L. Zhang, H. L. Li, Z. J. Zhang and Z. Sun, *J. Alloy. Compd.,* 2012, **519**, 149-155.

6 X. M. Zhang, F. G. Meng, H. Wei and H. Seo, *J. Ceram. Int.*, 2013, **39**, 4063-4067.

7 S. Chawla, T. Roy, K. Majumder, A. Yadav,*J. Exp. Nanosci.*, 2014, **9**, 776-784.

8 H. Y. Sun, X. Zhang, and Z. H. Bai,*J. Rare Earth*, 2013, **31**, 231-234.

9 W. D. Wang, J. K. Tang, S. T. Hsu, J. Wang and B. P. Sullivan, *Chem. Phys. Lett.*, 2008, **457**, 103-105.

10 Y. C. Jia, Y. J. Huang, Y. H. Zheng, N. Guo, H. Qiao, Q. Zhao, W. Z. Lv and H. P. You,*J.Mater. Chem.*, 2012, **22**, 15146–15152.

11 A. A. Setlur, R. J. Lyons, J. E. Murphy, N. P. Kumar and M. S. Kishore, *J. Solid State Sci. Technol.*, 2012, **2**, 3059-3070.

12 T. Moriga, Y. Sakanaka, Y. Miki, K. I. Murai and I. Nakabayashi,*Int. J. Mod. Phys. B*, 2006, **20**, 4159-4164.

13 J. M. Robertson, M. W. van Tol, W. H. Smits and J. P. H. Heynen, *Philips J.Res.*,1981, **36**, 15.

14 A. A. Setlur, W. J. Heward, Y. Gao, A. M. Srivastava, R. G. Chandran and M. V. Shankar,*Chem. Mater.*, 2006, **18**, 3314-3322.

15 M. M. Shang, J. Fan, H. Z. Lian, Y. Zhang, D. L. Geng and J. Lin, *Inorg. Chem.*, 2014, **53**, 7748−7755.

16 J. L. Wu, G. Gundiah and A. K. Cheetham,*Chem. Phys. Lett.*, 2007,**441**, 250-254.

17 A. Kalaji, P. J. Saines, N. C. George and A. K. Cheetham*Chem. Phys. Lett.*, 2013, **586**, 91–96.

18 N. C. George, A. J. Pell, G. Dantelle, K. Page, A. Llobet, M. Balasubramanian, G. Pintacuda, B. F. Chmelka and R. Seshadri, *Chem. Mater.*, 2013, **25**, 3979-3995.

19 T. Ebina, T. Iwasaki, A. Chatter, M. Katagiri and G. D. Stucky,*J. Phys. Chem. C*, 1997,**7**, 1125-1129.

20 L. V. Duong, B. J. Wood and J. T. Kloprogge,*Mater.Lett.,*2005, **59**, 1932-1936.

21 G. Gatana, W. Grunert, D. V. P. Van, E. F. Vansant, R. A. Schoonheydt and B. M. Weckhuysen, *J. Phys. Chem.*, 2000, **104**, 9195-9202.

22 G. Anoop, I. H. Cho, D. W. Suh, C. K. Kim and J. S. Yoo, *J. Lumin.*, 2013, **134**, 390-395.

23 L. A. O'Hare, B. Parbhoo and S. R. Leadley, *Surf. Interface Anal.*, 2004, **36**, 1427-1434.

24 S.D. Wolter, J. R. Piascik and B. R. Stoner, *Appl. Surf. Sci.*, 2011, **257**, 10177-10182.

25 J. Felsche,*The Crystal Chemistry of Rare-Earth Slicate*; Springer: Germany, 1973.

26 Z. X. Tao, Y. L. Huang and H. J. Seo, *Dalton T.*, 2013, **42**, 2121-2129.

27 G. Blasse and B. C.Grabmaier,*Luminescent material*; Springer: Germany, 1994.

28 W. R. Liu, C. H. Huang, C. P. Wu, Y. C. Chiu, Y. T. Yeh and T. M. Chen,*J. Mater. Chem.*, 2011, **21**, 6869-6874.

29 Z. P. Yang, G. W. Yang, S. L. Wang, J. Tian, X. N. Li, Q. L. Guo and G. S. Fu, *Mater. Lett.*,2008,**62**.1884-1886.

30 K. A. Denault, N. C. George, S. R. Paden, S. Brinkley, A. A. MIkhailovsky, J. Neuefeind, S. P. DenBaars and R. J, Seshadri, *J. Mater. Chem.*,2012, **22**, 18204-18213.